

## THE EFFECT OF VARIOUS NON-LINEAR MATRIX TYPES ON MECHANICAL PROPERTIES OF PARTICULATE COMPOSITE

ZDENĚK MAJER\*, and EVA NOVOTNÁ

Brno University of Technology, Technická 2896/2, 616 69  
Brno, Czech Republic  
majer@fme.vutbr.cz

Keywords: polymer composite, Young's modulus, rigid particles, non-linear matrix, FEM

### 1. Introduction

In this article polymeric particulate composites are studied. The polymeric particulate composites, especially with the polypropylene matrix (PP) and mineral fillers (rigid particles), are of great practical importance due to the possibility both of modifying many different mechanical properties and reducing the price/volume ratio of resulting material<sup>1,2</sup>. The properties of the matrix and rigid particles (especially size, shape and material properties) can have a significant effect on the global behavior of the composite. The change of the general material properties of the particulate composites (i. e. elastic modulus or yield stress) is the principal motivation for investigation composites filled by rigid particulate<sup>3</sup>.

Numerical calculations are considered a perfect homogeneous distribution of the particles in the matrix<sup>4,5</sup>.

### 2. Numerical model

The numerical model was created with respect a few general terms<sup>6</sup>: (i) particles should be of small size (less than 5  $\mu\text{m}$ ), (ii) aspect ratio must be close to unity to avoid high stress concentration, (iii) particles must debond prior to the yield strain of the matrix polymer in order to change the stress state of the matrix material and (iv) particles must be dispersed homogeneously in the polymer matrix.

The deformation behavior of a two-phase composite (soft matrix and rigid particle) with homogeneously distributed particles was numerically simulated on a microscopic scale using the finite element program ANSYS (see Fig. 1a). The finite element model was three dimensional with periodic boundary conditions on each side of the representative volume element model (RVE). The representative volume element was pulled from 27 unit cells. The calculated configuration corresponding to perfect adhesion between particles and matrix was considered. For simulations only one to eight model was used, see Fig. 1b.

For the numerical modeling the following assumptions were valid: the spherical shape of the particles, the regular distribution of the particles and the perfect adhesion between particle and matrix.

The mesh of finite elements was created using 20-node elements; this corresponds to the SOLID95 ANSYS element. In fact, the critical locations were situated at the boundary

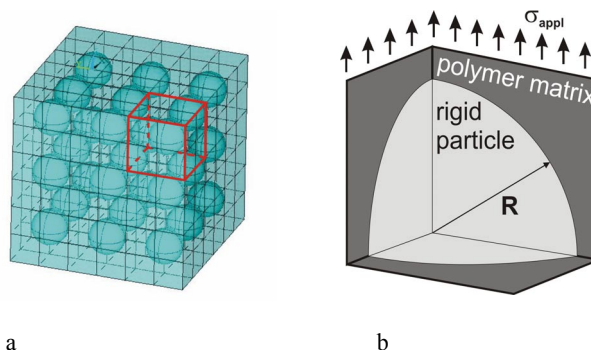


Fig. 1. a) Homogeneously distributed particles in representative volume element (RVE) considered for numerical simulations (one unit cell in red contour); b) one eighth of the unit cell = FEM model

between the particles and the matrix. The mesh was created to be more accurate in these zones and more dispersed in the matrix. The number of elements depends on the volume filler fraction (from pure matrix up to volume filler fraction 40 %); it was included between 100 000 and 300 000.

### 3. Experiment

The matrix of measured composite was copolymer PP SHAC KMT 6100 (produce by Shell International Chemical Co. Ltd.). This material is used for injection of various products (i. e. tools, cars components, equipment of household)<sup>7</sup>.

As rigid fillers were used magnesium hydroxide in two commercial available versions; company named KISUMA 5AU and MAGNIFIN H 10. In addition MAGNIFIN H 10 was modified by 2.5 % stearic acid named ASTRA. In fact, three different types of composites and pure matrix were measured (see Tab. I).

The ideal size of particles from experiment was determined too (see Fig. 2). According to Fig. 2 size dispersion was determined and it can be said that assumption of particle size 1  $\mu\text{m}$  was correct and valid.

Table I  
Different types of materials identification

Material	S	F2	F4	F6	S2	S4	S6	N2	N4	N6
Filler	---	KISUMA 5AU company modified			MAGNIFIN H 10 modified			MAGNIFIN H 10 unmodified		
[%] VFF	0	20	40	60	20	40	60	20	40	60

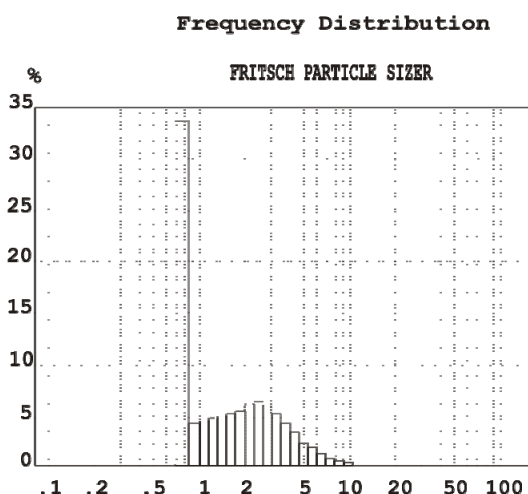


Fig. 2. Distribution of particles size for KISUMA 5AU filler

#### 4. Results and discussion

The polymeric particulate composites with the polypropylene matrix (PP) filled by mineral aggregates (rigid particles) were studied. Generally, the addition of rigid particles to a soft polymer matrix will have two main consequences. Firstly, the particulate composite will have out of doubt greater Young's modulus than self soft matrix. But secondly, rigid particles have an indispensable embrittling effect on the composite.

The presented work was focused mainly on the possibility of the particulate composite numerical modeling. Assuming that the particles in composite were regularly distributed in the matrix the Young's modulus for different types of composites was calculated. The configuration corresponding to

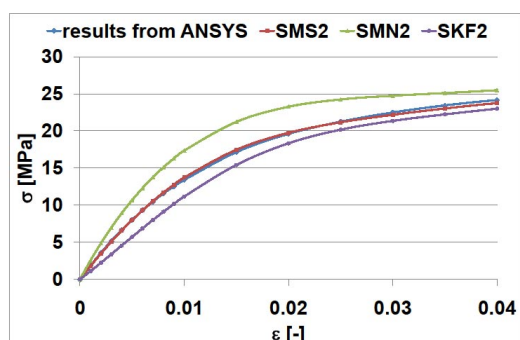


Fig. 3. Comparison of results from ANSYS with experimental data of composite different type for volume filler fraction 20 %

base matrix (matrix without particles) was considered as a special case.

The comparison between numerical results and experimental data was evaluated (see Fig. 3 for VVF = 20 %). Numerical results were calculated for three different types of composites (see Tab. I). Almost ideal congruity experimental data with numerical results for SMS2 composite (polypropylene with 20 % modified MAGNIFIN H 10) were found. Same composite but with unmodified particles had slightly higher value of Young's modulus. Composite with company modified particles KISUMA 5AU had moderate differences with comparison to SMN2 composite. It can be due to different type of acid for particles modification.

#### 5. Conclusions

It is shown that mechanical properties of particulate composite using numerical calculations can be use. We are able qualitatively very well estimate the Young's modulus of particulate composite for various volume filler fraction.

In the case of polymer matrix with 20 % particles is shown that numerical results are very close to particulate composite with modified particles MAGNIFIN H 10.

*This research was supported by grant P107/10/P503 of the Czech Science Foundation.*

#### REFERENCES

1. Pukánszky B.: Eur. Polymer J. 41, 645 (2005).
2. Nezbedová E.: Chem. Listy 101, 28 (2007).
3. Veselý P., Nezbedová E., Vlach B.: Chem. Listy 102, 1276 (2008).
4. Balac I., Milovancevic M., Tang Ch., Uskokovic P., Uskokovic D.: Mater. Lett. 58, 2437 (2004).
5. Jančář J., Kučera J., Veselý P.: J. Mater. Sci. 26, 4872 (1991).
6. Zuiderduin W. C. J., Westzaan C., Huétink J., Gaymans R. J.: Polymer 44, 261 (2003).
7. Molíková E.: Ph.D. Thesis (2003) (in czech).

**Z. Majer, and E. Novotná<sup>a</sup>** (Institute of Solid Mechanics, Mechatronics and Biomechanics, <sup>a</sup>Institute of Materials Science and Engineering, Brno, Czech Republic): **The Effect of Various Non-Linear Matrix Types on Mechanical Properties of Particulate Composite**

The main objective of this contribution is the numerical investigation of the properties in polymeric particulate composite. The composite was modeled as a two-phase continuum (using representative volume element) and numerically simulated on a microscopic scale using finite elements method (ANSYS). For calculations of the composite Young's modulus finite element model with respect the elastic-plastic model of polymer matrix (polypropylene) was used. The numerical results with experimental data were confronted as well as the data for modeling of primary matrix was determinate from experiment.

## THE INFLUENCE OF SUBSTRATE BIAS ON NANOHARDNESS OF a-C:N FILMS DEPOSITED ON CoCrMo ALLOY

MARIÁN MARTON<sup>a</sup>, DAVID KOVALČÍK<sup>a</sup>,  
EVA ZDRAVECKÁ<sup>b</sup>, MARIÁN VARGA<sup>a</sup>,  
LENKA GAJDOŠOVÁ<sup>a</sup>, ERIK VAVRINSKÝ<sup>a</sup>,  
MARIAN VESELÝ<sup>a</sup>, ROBERT  
REDHAMMER<sup>a</sup>, and MARCUS HOPFELD<sup>c</sup>

<sup>a</sup> KME FEI STU in Bratislava, Ilkovičova 3, 812 19 Bratislava, <sup>b</sup> Department of Technologies and Materials, FME TU of Košice, Mäsiarska 74, 040 01 Košice, Slovak Republic, <sup>c</sup> Ilmenau university of technology, Institute of materials engineering, Ilmenau, Germany  
marian.marton@stuba.sk

Keywords: DLC, Carbon nitride, Nanohardness, Raman spectroscopy, CoCrMo

### 1. Introduction

The biocompatibility along with mechanical properties and corrosion behavior plays an important role in feasibility of biomedical implants. Diamond like carbon seems to be the promising material in which all these requirements can be achieved. Covering the surface of artificial joints and implants by DLC thin film may lead to extension of lifetime of the implants, improvement of implants acceptance by human body and decrease of the organism immune system inflammation reactions<sup>1</sup>. The mechanical properties of DLC are directly affected by sp<sup>3</sup>/sp<sup>2</sup> ratio. It is known that, the incident carbon ions energy is the key factor affecting the atoms hybridization. The application of substrate bias is frequently used to control the energy around 100 eV to promote the formation of sp<sup>3</sup> bonds in the film<sup>2,3</sup>. In this study nitrogen doped amorphous carbon (a-C:N) films were deposited on medical grade CoCrMo alloy. The influence of negative substrate bias on the thin films nanohardness was investigated.

### 2. Experimental

a-C:N thin films were deposited on cylindrical CoCrMo samples in a vacuum system UVNIPA-1-001 described previously<sup>4</sup> using a pulsed arc source for sputtering the graphite target. The substrates were cleaned for 10 min. with Ar ions prior to the deposition cycle. The sputtering frequency of the arc source pulses was 3 Hz and the total number of sputtering pulses was 3000. Background pressure was 10<sup>-4</sup> Pa and working pressure was maintained at around 1 Pa according to gas flow. Argon to nitrogen (Ar/N) gas flow ratio was set up to 40/40 sccm. The temperature was kept below 150 °C. Negative substrate bias from 0 to -2.5 kV was applied during deposition process. Hardness measurements were performed using Fisher Picodentor HM500. The structural properties of a-C:N films were studied by Raman spectroscopy with 632.8 nm radiation from a He-Ne laser. The Raman spectra

were fitted with a Gaussian line to obtain the D and G peak positions and I<sub>D</sub>/I<sub>G</sub> ratio.

### 3. Results and discussion

The Raman spectra for a-C:N films deposited with different substrate bias are shown in Fig. 1. Spectra of the films deposited under different conditions contain the typical diamond-like carbon D and G broad peaks attributed to the disorder-allowed optical zone mode (A<sub>1g</sub>) of microcrystalline graphite sheets and optically allowed zone (E<sub>2g</sub> mode) of the aromatic ring in graphite, sp<sup>2</sup> coordinated C-C bonds, C-N bonds and sp<sup>2</sup> C-N bonds, respectively<sup>5</sup>. The D peak arises owing to the limitation in the graphite domain size induced by grain boundaries or imperfections, such as substitutional N atoms and sp<sup>3</sup> coordinated carbon and nitrogen atoms.

A remarkable change in G peak position and I<sub>D</sub>/I<sub>G</sub> ratio with varying substrate bias can be observed in Fig. 2. The G peak position decreases from 1537 cm<sup>-1</sup> to 1525 cm<sup>-1</sup> with increasing negative substrate bias from 0 to -2.5 kV. As the incident carbon ion energy due to changing substrate bias increases, the I<sub>D</sub>/I<sub>G</sub> ratio decreases from 0 V and has a minimum value around -2 kV and then again increases. Robertson reported that, the I<sub>D</sub>/I<sub>G</sub> falls as the number of rings per cluster falls and the fraction of chain groups (disorder) rises. The I<sub>D</sub>/I<sub>G</sub> is also in direct proportion to in-plane correlation length L<sub>a</sub> or domain size<sup>3</sup>. The increase of substrate bias leads to a rise in carbon ion kinetic energy that promotes the carbon ion bombardment on the substrate surface during the film deposition and favors the formation of sp<sup>3</sup> carbon bonding. However, when the ion energy is too high, the ions may damage the films surface and cause sp<sup>3</sup> bonds to transform into sp<sup>2</sup> bonds<sup>6,7</sup>.

Fig. 3 shows the dependence of hardness and G peak full width at half maximum (FWHM) on negative bias for a-C:N on CoCrMo. We can see that the hardness has its maximum between 1 kV and 2 kV, whereas the G peak width decreases nearly linear. High hardness can be reached using the optimum ion energy for the formation of high concentration of sp<sup>3</sup> C-C and C-N bonds in the a-C:N film.

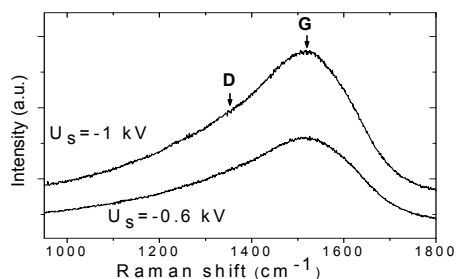


Fig. 1. Typical Raman spectra of a-C:N on CoCrMo deposited with different negative substrate bias

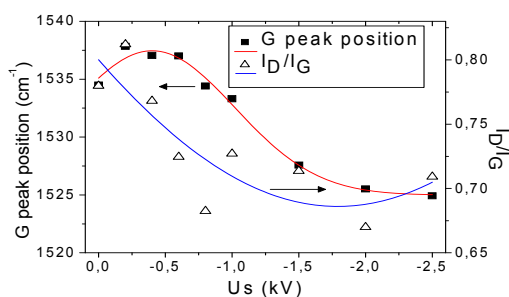


Fig. 2. Dependence of Raman G peak position and  $I_D/I_G$  ratio of a-C:N deposited with different substrate bias

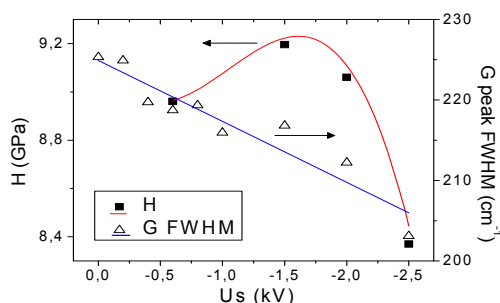


Fig. 3. Dependence of hardness and  $I_D/I_G$  ratio of a-C:N deposited with different substrate bias

#### 4. Conclusions

Diamond like carbon thin films were deposited on medical grade CoCrMo alloys by glow discharge sputtering method with different substrate biasing and gas flow. Hardness of the coated samples was dependent on the value of connected negative substrate bias. The highest hardness on CoCrMo substrates was measured for negative bias between 1 kV and 2 kV, where the Raman spectroscopy showed the lowest  $I_D/I_G$  ratio and G peak position.

This work was done in Center of Excellence CENAM-OST (Slovak Research and Development Agency Contract No. VVCE-0049-07) and was financially supported also by grants APVV-0628-06, APVV-0548-07, SK-CZ-0139-09, LPP-0094-09, LPP-0246-06, LPP-0149-09, and VEGA 1/0807/08, 1/0857/08, 1/0390/08.

#### REFERENCES

1. Choi H. W., Lee K.-R., Park S. J., Wang R., Kim J.-G., Oh K. H.: *Surf. Coat. Technol.* 202, 2632 (2008).
2. Lifshitz Y.: *Diamond Relat. Mater.* 8, 1659 (1999).
3. Robertson J.: *Mater. Sci. Eng. R37*, 29 (2002).
4. Marton M., Zdravecká E., Vojs M., Izák T., Veselý M., Redhammer R., Varga M., Šatka A.: *Vacuum* 84, 65 (2010).
5. Sui J. H., Zhang Z. G., Cai W.: *Nuclear Instruments and Methods in Physics Research B* 267, 2475 (2009).
6. Surdu-Bob C., Vladioiu R., Badulescu M., Musa G.: *Diamond Relat. Mater.* 17, 1625 (2008).
7. Sui J. H., Gao Z. Y., Cai W., Zhang Z. G., *Mater. Sci. Eng. A* 454–455, 472 (2007).

M. Marton<sup>a</sup>, D. Kovalčík<sup>a</sup>, E. Zdravecká<sup>b</sup>, M. Varga<sup>a</sup>, L. Gajdošová<sup>a</sup>, E. Vavrinský<sup>a</sup>, M. Veselý<sup>a</sup>, R. Redhammer<sup>a</sup>, and M. Hopfeld<sup>c</sup> (<sup>a</sup>KME FEI STU in Bratislava, <sup>b</sup>Department of Technologies and Materials, FME TU of Košice, Košice, Slovak Republic, <sup>c</sup>Ilmenau university of technology, Institute of materials engineering, Ilmenau, Germany): **The Influence of Substrate Bias on Nanohardness of a-C:N Films Deposited on CoCrMo Alloy**

In this study nitrogen doped amorphous carbon (a-C:N) films were deposited on medical grade CoCrMo alloy substrates by vacuum glow discharge sputtering technique from graphite target using different deposition conditions. The influence of negative substrate bias on the thin films nanohardness was investigated. The structural properties of a-C:N films were evaluated by Raman spectroscopy.

## NANOINDENTATION INTO PMMA AND FUSED SILICA BY SPHERICAL AND POINTED INDENTERS – A COMPARISON

JAROSLAV MENCÍK<sup>a</sup>, and JIŘÍ NOHAVA<sup>b</sup>

<sup>a</sup> University of Pardubice, Studentská 95, 532 10 Pardubice, Czech Republic, <sup>b</sup> CSM Instruments, Rue de la Gare 4, CH-2034 Peseux, Switzerland  
jaroslav.mencik@upce.cz

Keywords: Nanoindentation, spherical indenter, pointed indenter, viscoelasticity, calibration

### 1. Introduction

The paper compares characteristic features of low-load indentation into two different homogeneous materials: fused silica and polymethyl-methacrylate. FS has high elastic modulus and hardness, and its response to load is instantaneous. PMMA is more compliant, with response depending also on time. For each material, two indenters were used: pointed, with high stresses, leading always to irreversible deformations, and spherical, where the stresses grow gradually. Under low loads, fully reversible deformations thus can be attained, suitable for the study of elastic or viscoelastic properties.

### 2. Experiments

All tests were done by nanoindenters NHT and UNHT from CSM Instruments, Switzerland, with a Berkovich indenter and a spherical indenter of nominal radius  $R = 200 \mu\text{m}$ .

#### 2.1. Polymethyl-methacrylate (PMMA)

Creep tests and load-unload tests were done with a spherical indenter and a Berkovich indenter.

##### Creep test with a spherical indenter

The load grew to the nominal value  $F = 5.12 \text{ mN}$  during 5.7 s and then it was held constant till indenter stopping ( $\approx 1050 \text{ s}$ , Fig. 1). The growth of indenter depth in time,  $h(t)$ , was approximated by a model consisting of a spring ( $C_0$ ) in series with three Kelvin-Voigt bodies<sup>1</sup>:

$$[h(t)]^m = K F \{ C_0 - \sum C_j [1 - \rho_j \exp(-t/\tau_j)] \} \quad (1)$$

where  $m = 3/2$ ,  $K = 3/(4\sqrt{R})$ , and constants  $C_1, C_2, \dots, C_n$  are compliances pertaining to the relaxation times  $\tau_j$ ;  $n = 3$ . The constants  $\rho_j = (\tau_j/t_R)[\exp(t_R/\tau_j) - 1]$  correct the fact of that the load grows to the nominal value during some time  $t_R$ ; see Ref.<sup>2</sup>. The instantaneous compliance  $C_0$  is related to the reduced instantaneous modulus as:

$$C_0 = 1/E_r \quad (2)$$

$E_r$  is related to the specimen modulus  $E$  and indenter modulus  $E_i$  as  $1/E_r = [(1 - \nu^2)/E + (1 - \nu_i^2)/E_i]$ ;  $\nu$  is the Poisson's ratio. The constants were as follows:

$C_0 = 2.75 \cdot 10^{-10}$ ,  $C_1 = 2.29 \cdot 10^{-10}$ ,  $C_2 = 1.72 \cdot 10^{-10}$ ,  $C_3 = 1.10 \cdot 10^{-10}$  (all  $\text{m}^2/\text{N}$ ),  $\tau_1 = 1.6 \text{ s}$ ,  $\tau_2 = 19.5 \text{ s}$ ,  $\tau_3 = 195.0 \text{ s}$ .

The reduced instantaneous elastic modulus  $E_r$ , calculated via Eq. (2) as  $1/C_0$ , is  $E_r = 3.64 \text{ GPa}$ .

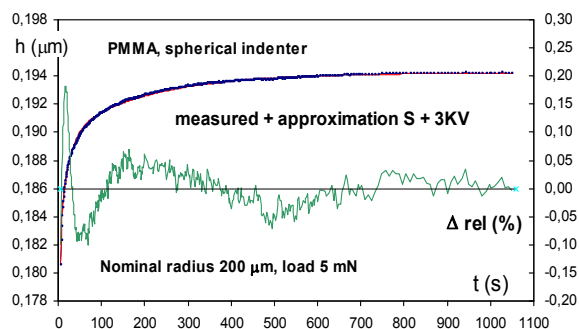


Fig. 1. Indentation creep of PMMA under constant load.  $\Delta \text{rel}$  – relative difference between the measured and calculated values

The apparent reduced modulus was also calculated from the depth of penetration using Hertz formula<sup>3</sup>

$$E_r = (3/4) F R^{-1/2} h^{-3/2} \quad (3)$$

In this case,  $E_r$  was 3.53 GPa for the end of load growth (depth  $h = 181 \text{ nm}$ ), and 3.18 GPa for the end of dwell under constant load (with  $h = 194 \text{ nm}$ ).

The mean contact pressure, calculated from<sup>3</sup>

$$p_m = \pi^{-1} [(16/9) F E_r^2 R^2]^{1/3} \quad (4)$$

for  $F = 5.12 \text{ mN}$ ,  $E_r = 3.6 \text{ GPa}$  and  $R = 200 \mu\text{m}$ , was only  $p_m = 45.7 \text{ MPa}$ . For such low stresses, the deformations were mostly viscoelastic and reversible.

##### Creep test with Berkovich indenter

The load increased during 18 s to  $F = 201 \text{ mN}$  and then it was held constant 3700 s, without a sign of indenter stopping. The indenter displacement  $h(t)$  during the dwell was fitted by several rheological models. The constants were again calculated from Eq. (1), now with  $m = 2$  and  $K = \pi/(2 \tan \alpha)$ . Similarly good fits were obtained by the model „Spring + Dashpot + 2Kelvin-Voigt bodies” and „S+3KV”. However, the contact pressure was much higher than under spherical indenter and caused irreversible plastic and viscous deformations. Thus, the S+D+2KV model is more appropriate. For the same reason, also the „instantaneous” compliances ( $C_0 = 2.9\text{--}3.1 \cdot 10^{-10} \text{ m}^2/\text{N}$  for the model S+D+2KV, and  $3.4\text{--}4.0 \cdot 10^{-10} \text{ m}^2/\text{N}$  for S+3KV) were higher than in the low-load tests with spherical indenter. Thus, elastic modulus cannot be determined in this way.

### Load-unload tests with Berkovich indenter

The load increase to the nominal force of 300 mN lasted 23 s, the dwell under nominal load lasted 62 s, and the unloading lasted 20.6 s; the maximum depths were 8.12–8.20  $\mu\text{m}$ . The elastic reduced modulus  $E_r$ , was calculated using Oliver & Pharr<sup>4</sup> approach:

$$E_r = (\pi^{1/2} / 2\beta) S/A^{1/2} \quad (5)$$

where  $S = dF/dh$  is the contact stiffness at the beginning of unloading,  $A$  is the contact area calculated from the contact depth  $h_c$  ( $= h - 0.75F/S$ ), and  $\beta$  is a constant ( $\beta = 1$  for spherical indenter and 1.034 for Berkovich one).

In five tests<sup>1</sup>,  $E_r$  varied between 3.62–3.67 GPa, close to the values from creep tests with Berkovich indenter. These values were also close to those obtained by J.M. for sheet PMMA in bending tests with relatively fast loading (3.7–3.9 GPa at 0.45 s, decreasing to 3.0 GPa after 1000 s).

Mean contact pressure (hardness), obtained from load-unload tests with Berkovich indenter<sup>1</sup> was about 205 MPa. This value has caused irreversible viscoplastic deformations in the polymer.

## 2.2. Fused silica

### Tests with Berkovich indenter

A simple load-unload cycle was used, with the parameters: 32 s increase to the maximum load  $F = 20.1$  mN, 15 s dwell, and unloading to 0; the maximum depth was  $h = 433$  nm. The reduced modulus, calculated using Oliver & Pharr approach, was  $E_r = 70.9$  GPa. The mean contact pressure (hardness) was  $H = 9.99$  GPa.

### Tests with a spherical indenter

A load-unload cycle as above was used, with two nominal loads: 51.4 mN and 5.0 mN. For  $F = 51.4$  mN, the depth was  $h = 132.7$  nm. The modulus, determined according to O&P, was  $E_r = 60.0$  GPa, and the contact mean pressure  $p_m$  (hardness  $H$ ) was 641.7 MPa.  $E_r$  was also calculated from the maximum indenter displacement using Hertz' formula (3), with the result  $E_r = 56.4$  GPa.

For the lower load, 5.02 mN, the depth was  $h = 37.0$  nm, and the reduced modulus (Oliver&Pharr<sup>4</sup>) was  $E_r = 47.7$  GPa and mean contact pressure  $p_m = 163.2$  MPa. The reduced modulus via Eq. (3) was 37.4 GPa. The contact pressure was much lower than the yield stress  $Y$  for fused silica (several GPa), and the deformations were only elastic.

### Indenter calibration

The elastic modulus of fused silica (FS), obtained from the tests with spherical indenter, was significantly lower than literature values ( $E_r \approx 70$  GPa). In our calculations, the tip radius  $R = 200$   $\mu\text{m}$  was assumed. However, it is known that for small radii the tip shape often deviates from an ideal sphere. If – vice versa – the elastic modulus of the sample is known, it is possible to calculate the apparent (or effective) radius corresponding to the load and penetration.

For example, for  $F = 51.4$  mN,  $h = 132.7$  nm and  $E_r = 70$  GPa, the effective tip radius is  $R = 134$   $\mu\text{m}$  (instead of 200  $\mu\text{m}$ ). In this way, the calibration curve, giving the effective radius as a function of penetration depth,  $R_{\text{eff}}(h)$ , may be constructed from the  $F(h)$  curve as<sup>5</sup>

$$R_{\text{eff}}(h) = (9/16) F^2 E_r^{-2} h^{-3} \quad (6)$$

Fig. 2 shows the calibration curve made for this indenter on FS under the assumption  $E_r = 70$  GPa.

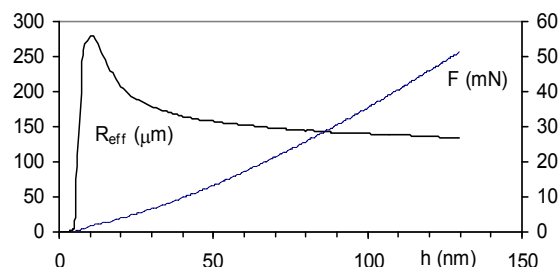


Fig. 2. Effective radius  $R_{\text{eff}}$  of the spherical indenter as a function of penetration  $h$ . Nominal radius  $R = 200$   $\mu\text{m}$ . Thin curve:  $F(h)$

## 3. Discussion and conclusions

Stresses below a spherical indenter grow gradually with indenter load, and can thus be kept below the onset of irreversible changes. The elastic modulus of PMMA, obtained in this way by spherical indenter, was similar to the values obtained by other means.

For fused silica, the elastic modulus obtained with spherical indenter for very small depths of penetration, differed significantly from the known values. A reason may be the tip deviation from ideal shape. Calibration of spherical indenters is thus necessary. This issue exceeds the scope of this paper (a role can also be played by the indented material) and will be studied more in the future.

*This work was supported partly by the Grant Agency of Czech Republic, projects No. GAČR 103/08/1340 and GAČR 103/08/1197.*

### REFERENCES

1. Menčík J., He L. H., Němeček J.: *Polym. Test* 30, 101 (2010).
2. Oyen M.: *Philos. Mag.* 86, 5625 (2006).
3. Johnson K. L.: *Contact mechanics*. Cambridge University Press, Cambridge 1985.
4. Oliver W. C., Pharr G. M.: *J. Mater. Res.* 7, 1564 (1992).
5. Menčík J.: *Chem. Listy* 105, s680 (2011).

**J. Menčík<sup>a</sup>, and J. Nohava<sup>b</sup>** (<sup>a</sup> *University of Pardubice, Czech Republic*, <sup>b</sup> *CSM Instruments, Switzerland*): **Nanoindentation into PMMA and Fused Silica by Spherical and Pointed Indenters – a Comparison**

The paper compares characteristic features of low-load indentation into two different materials: fused silica and polymethyl-methacrylate. FS has high hardness and elastic modulus, and instantaneous response to load. PMMA is more compliant, with response depending also on time. For each material, two indenters were used: pointed, with high stresses, causing always irreversible deformations, and spherical with gradual stress growth.

## INFLUENCE OF STRAIN RATE ON AUTOMOTIVE STEEL SHEET BREAKING

**MÁRIA MIHALIKOVÁ\***, MIROSLAV NÉMET, PAVOL ZUBKO, and MAREK VOJTOKO

*Department of Materials Science, Faculty of Metallurgy,  
Technical University of Košice, Letná 9, 042 00 Košice, Slo-  
vak Republic  
maria.mihalikova@tuke.sk*

Keywords: automotive steel sheet, dynamic tests

### Introduction

Strain rate is a significant external factor and its influence on material behavior in forming process is a function of its internal structure<sup>1,2</sup>. Increasing strain rate increases material's resistance against deformation, but also increases tendency to brittle fracture. Increasing strain rate results in changes to the microstructure and substructure of deformed material.

In practical terms, this means that it is necessary to know the impact of strain rate on mechanical properties of specific material, which are the basis for the calculation of the deformational resistance, but also the processes taking place during forming.

Prediction of strain rate impact on material's properties is quite complicated. It is related to the fact that intensity of strain rate impact is a function of material's internal structure, and also the interpretation of test results is very difficult at high rates.

Increasing strain rate also increases the critical flow stress, yield strength grows strongly, tensile strength increases, and deformation characteristics of the material are changed<sup>3–9</sup>. At the same time also values of forming criteria derived from these characteristics are changed<sup>5,6</sup>.

### 2. Experimental material and methods

Experiments were performed on samples taken from the cold rolled strips and then hot dip galvanized H340 LAD grades intended for the production of stampings in automotive industry.

The tested material was 1.0 mm thick. Samples of the material were taken in rolling direction and flat test specimens for tensile test were produced. Tensile test was carried out on INSTRON 1185 tensile testing machine at loading speed of 1–1000 mm min<sup>-1</sup>. Dynamic tests were carried out on PSW type pendulum impact tester at max. speed of 24 m s<sup>-1</sup>.

### 3. Results and discussion

According to references<sup>3,4</sup>, increasing strain rate increases the resistance of tested steel to plastic deformation, yield strength and tensile strength increase (Fig. 1).

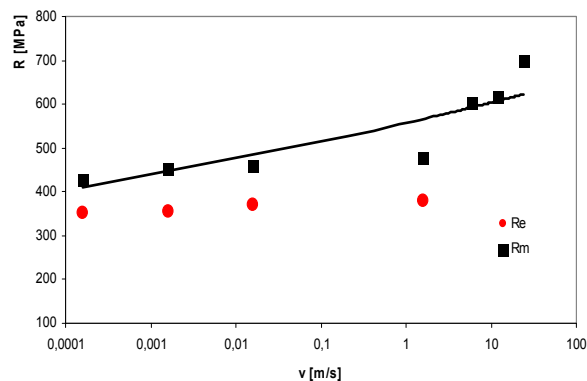


Fig. 1. Effect of loading rate on the yield stress  $R_e$  and the tensile ultimate strength  $R_m$  of steel H340 LAD

In the static loading is progress of  $R_m$  linear. For the dynamic speeds is observed high growth of  $R_m$ .

At static loading speed of  $1.6 \times 10^{-4}$  m s<sup>-1</sup> a transcrystalline ductile failure with dimple morphology can be observed on fracture surface, while the shape and symmetry of dimples is related to the stress at failure spot. The size and layout of the dimples depends on the grain size. At low rates, (Fig. 2) it is a ductile failure with equiaxial dimple morphology, where the dimples are deep.

The generation of fracture surface is accompanied by significant plastic deformation associated with increasing the number of active slip systems at a higher strain rate. Fracture surface obtained at loading speed of  $1.6$  m s<sup>-1</sup> has similar characteristics (Fig. 3).

On the fracture surface, the number of secondary cracks and voids that are generated in direction of lines, has increased. Increase of plastic deformation is clear from the shape of dimples. Dimples are elongated with a strong presence of striation on the walls. Coalescence of cavities is seen

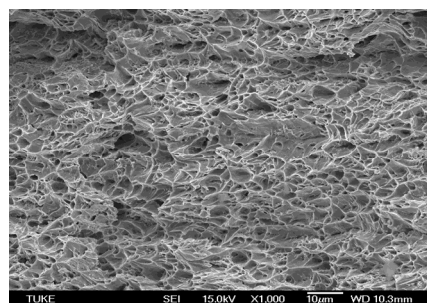


Fig. 2. Fracture surface at a loading rate  $1.6 \times 10^{-4}$  m s<sup>-1</sup>

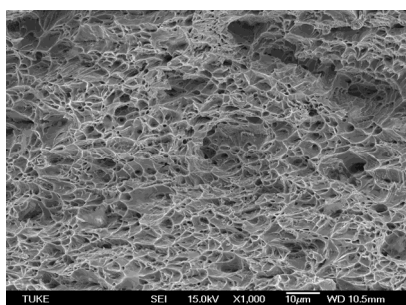


Fig. 3. Fracture surface at a loading rate 1.6 m s<sup>-1</sup>

more significantly in direction perpendicular to tensile stress direction. At loading speed of 24 m s<sup>-1</sup>, the angle of rupture increases (Fig. 4), uneven surface is generated, dimples are shallower. At the void growth in the process of ductile failure, coalescence bridges are getting narrow. Bridges are breaking by gradual stretching. Formation of ductile fracture takes place in the phase of micro-defect nucleation, void growth and contraction of bridges between the voids. Micro-defects nucleation in ductile failure was generated by decohesion of inclusions and other particles from the matrix.

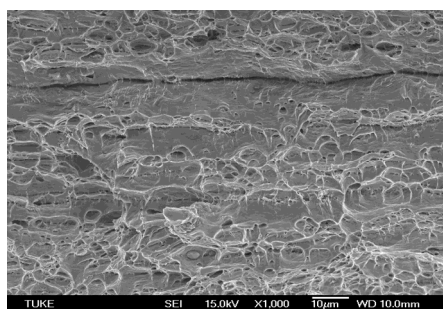


Fig. 4. Fracture surface at a loading rate 24 m s<sup>-1</sup>

Microscopic observation of strain-strengthened steel structure confirmed that with increasing strain rate, also inhomogeneity of deformation plasticity increases in the volume of deformed steel. It follows that the resulting properties of strain-strengthened material are influenced by strain rate.

#### 4. Conclusion

The document analyzes the impact of strain rate of H340 LAD steel sheet on the change of mechanical properties and fracture appearance. Based on the results of tensile tests and dynamic tests at the loading speed range from  $1.6 \times 10^{-4} \text{ m s}^{-1}$  to  $24 \text{ m s}^{-1}$  for the tested steel, it can be stated:

- At increasing strain rate up to about  $3 \text{ s}^{-1}$ , there is no deterioration in material characteristics of deep drawing, but deformation resistance increases.
- In case of the tested HSLA steel of H340 LAD grade it is the ductile failure, which is generated by void mechanism.
- At all speeds (rates), the material fails by transcrystalline ductile fracture with dimple morphology.
- With the increasing strain rate, plastic deformation becomes more significant and there is greater number of voids that are oriented in the direction of lines, dimples are shallower.

*This study was supported by the Grant Agency of Slovak Republic, grant project APVV No. 0326-07.*

#### REFERENCE

1. Michel' J., Buršák M.: *Komunikacie* 5, 34 (2004).
2. Lis J., Lis A., Kolan K.: *J. Mater. Process. Technol.* 162, 350 (2005).
3. Čížmarová E., Michel' J.: *Acta Metallurgica Slovaca* 9, 90 (2003).
4. Michel' J., Buršák M., Mihaliková M.: *Acta Metallurgica Slovaca* 11, 134 (2005).
5. Wang H. R., Wang W., Gao J. O.: *Mater. Lett.* 64, 219 (2010).
6. Zhao H., Gary G.: *Mater. Sci. Eng. A* 207, 46 (1996).
7. Buršák M., Mamuzič I., Michel' J.: *Metalurgija* 46, 37 (2007).
8. Vadasová Z., Mihaliková M.: *J. Metals, Mater. Minerals* 16, 15 (2006).
9. Kormaníková E., Kotrasová K.: *J. Int. Sci. Publ. Mater., Methods & Technologies* 3, 117 (2009).

**M. Mihaliková, M. Némec, P. Zubko and M. Vojtko**  
*(Department of materials science, Faculty of metallurgy, Technical University of Košice, Slovakia): Impact of Strain Rate on Automotive Steel Sheet Breaking*

This analysis is aimed at impact of loading speed from  $1.6 \times 10^{-4} \text{ m s}^{-1}$  to  $24 \text{ m s}^{-1}$  on changes in breaking of steel sheet used for automotive body components. Experiments were performed on samples taken from H340 LAD grade strips produced by cold rolling and hot dip galvanizing. Material strength properties were compared based on measured values, and changes to fracture surface character were observed.

## THE INFLUENCE OF SURFACE PROTECTION ON CORROSION RESISTANCE OF ALUMINIUM ALLOY

**ANETA NĚMCOVÁ<sup>\*a</sup>, MARTIN ZMRZLÝ<sup>b</sup>,  
and BOHUMIL PACAL<sup>a</sup>**

<sup>a</sup> Institute of Material Science and Engineering, Faculty of Mechanical Engineering, Brno University of Technology, Technická 2, Brno, <sup>b</sup> Institute of Materials Science, Faculty of Chemistry, Brno University of Technology, Purkyňova 118, Brno, Czech Republic  
ynemco00@stud.fme.vutbr.cz

Keywords: aluminium alloy, corrosion, salt spray test, coating, surface protection

### 1. Introduction

The resistance of Al against corrosion in aqueous media can be attributed to a rapidly formed surface oxide film, which is composed of  $\text{Al}_2\text{O}_3$ ,  $\text{Al}(\text{OH})_3$  and  $\text{AlO}(\text{OH})$  phases. Nevertheless, the presence of aggressive ions like chlorides causes significant attack<sup>1,2</sup>. The main corrosion process that is developed on the surface of Al alloys in a NaCl solution is the localized alkaline corrosion in the Al matrix surrounding Al (Mn, Fe, Cr) cathodic intermetallics<sup>3</sup>.

In this work is compared the corrosion resistance of AlCu4Mg1 alloy in the basic state and with surface treatment used for protection against extraneous influences in the aircraft industry. This is due to extreme danger of accidents if the local corrosion attack induces a reduction in strength (e.g. in the rivet joints).

### 2. Experimental material

The experimental material was received as a L-beam with dimensions  $14 \times 14$  mm with length 150 mm and thickness 2 mm. The chemical composition was measured by glow discharge optical emission spectroscopy (GDOES) using Spectrumat GDS-750 device (see Tab. I).

Further material under study was the same alloy, however with protective coating. Fig. 1 shows microstructure of this material with coating containing organic polymer (epoxy resin with unspecific mineral fiber and aluminium particles).

Table I

The chemical composition in wt.% of AlCu4Mg1 alloy

Si	Fe	Cu	Mn	Mg	Zn	Ti	Al
0.21	0.31	4.10	1.08	1.71	0.03	0.02	Balance

### 3. Experimental procedure

For the assessment of the corrosion behaviour of the specimens of an Al alloy in a spray of neutral aqueous solution of sodium chloride the corrosion chamber Angelantoni

DCTC 600 P was used. The course of the corrosion resistance test was in accordance with the standard EN ISO 9227 (ref.<sup>4</sup>). The experiments were carried out with increasing exposition time of 48, 96, 240, 480, 720 and 1000 hrs. Every cycle was conducted in the test environment of 5% NaCl aqueous solution with pH 6.9 and temperature  $35 \pm 2$  °C.

Final cleaning of the specimens after exposition was carried out by dipping in a solution of  $\text{CrO}_3 + \text{H}_3\text{PO}_4 + \text{H}_2\text{O}$ ; according to Czech standard ČSN 03 8452 (ref.<sup>5</sup>). The weight loss was measured at analytical balances ( $d = 0.1$  mg) after each experiment and calculated in  $\text{g m}^{-2}$  and  $\text{mm}^3/\text{year}$ .

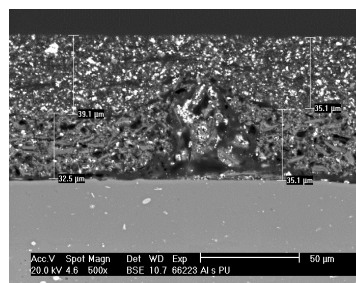


Fig. 1. The AlCu4Mg1 alloy with protective coating, SEM

### 4. Results

The corrosion rate calculated from weight losses versus time exposure are presented in Fig. 2.

Metallographic evaluation was performed according to applicable standard ČSN 03 8137 (ref.<sup>6</sup>). The corrosion attack after representative time of exposition observed by scanning electron microscope on metallographic cross-section cuts is shown in Fig. 3.

The results of local chemical analysis of the friable layer of corrosion products on specimens after 168 h exposure on spots 1 and 2 in Fig. 4 are presented in Tab. II. XRD analysis revealed presence of,  $\text{Al}(\text{OH})_3$  and large amount of non-

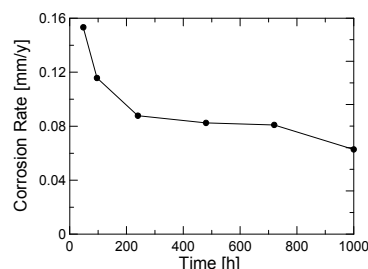


Fig. 2. Corrosion rate of AlCu4Mg1 as a function of exposure time in corrosion chamber

crystalline phase, that can be ascribed to mixture of hydrated compounds, including hydrated chlorides of substrate elements etc. There was no corrosion attack observed after 1000 hours exposure on the specimens with protective coating.

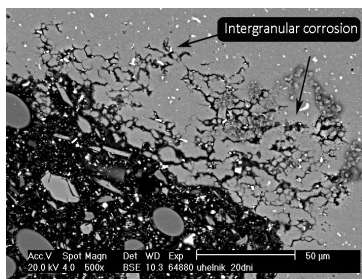


Fig. 3. Corrosion attack after exposure 480 hours, the AlCu4Mg1 alloy without protective coating, SEM

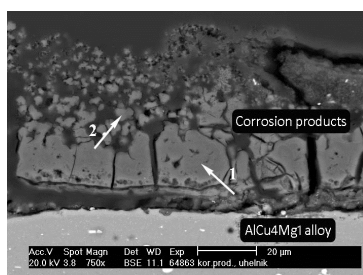


Fig. 4. The corrosion products on AlCu4Mg1 alloy after 168 hours exposure, SEM

Table II

The local chemical analysis by EDX of corrosion products on the surface of AlCu4Mg1 alloy

	Al [wt.%]	O [wt.%]	Cl [wt.%]
Spot 1	39.7	58.7	1.6
Spot 2	38.7	56.4	4.9

## 5. Discussion

The AlCu4Mg1 alloy was used for testing in neutral salt spray test. The chemical analysis by EDX has shown that the structure composed phases based on Al-Cu-Mg and Al-Cu-Fe-Mn.

The dependence of corrosion rate on exposure time (see Fig. 2) shows the greatest drop between 48 and 240 hours. Further progress was only slightly decreasing. This is type of corrosion when the corrosion attack is markedly localized. The corrosion pits are then filled by corrosion product that act as the partial barrier between metal and corrosion environment.

Pitting was observed after every exposure time with different average depth. Some differences were also observed in the depth on the edges and on the planes. After time of 480 hours and longer the intergranular corrosion (see Fig. 3) started to occur besides the corrosion pitting. The intergranular corrosion progressed along the grain boundaries and was observed mainly below the surface, starting from the edges of specimens.

Fig. 1 shows experimental material with protective coating. There wasn't observed any corrosion attack even after 1000 hours exposure on these specimens.

## 6. Summary and conclusions

The AlCu4Mg1 alloy was used for salt spray tests in 5% NaCl aqueous solution with neutral pH. The dependence of corrosion rate on exposure time shows the greatest decrease between 48 and 240 hours and further progress was only slightly decreasing. Metallographic evaluation of corrosion attack identified corrosion pitting after every time of exposition and the intergranular corrosion after 480 hours and longer. The main cause of its occurrence was the evolution of corrosion microcells between the matrix and the Al<sub>2</sub>CuMg phase which has a cathodic behaviour in the particular environment.

There was no corrosion attack was observed on specimens with protective coating even after 1000 hours exposure.

Result of this work will be utilized for detailed research of strength of rivet joints after corrosion degradation. Morphology and form of corrosion attack will be very useful for explanation of strength differences at microstructural scale.

*This research was supported by project of MIT of the Czech Republic no. FR TI 1/274 and project of the MEYS of the Czech Republic no. IM2560471601.*

## REFERENCES

- Ghali E.: *Corrosion resistance of Aluminium and Magnesium Alloy*. p. 719. Wiley 2010.
- Mishra A. K., Balasubramaniam R.: *Mater. Chem. Phys.* 103, 385 (2007).
- Szklarska-Smialowska Z.: *Corros. Sci.* 41, 1743 (1999).
- ČSN EN ISO 9227. Prague (2007).
- ČSN 03 8452. Prague (1989)
- ČSN 03 8137. Prague (1990).

**A. Němcová, M. Zmrzlý, and B. Pacal** (*Brno University of Technology, Czech Republic*): **The Influence of Surface Protection on Corrosion Resistance of Aluminium Alloy**

This paper deals with the corrosion resistance of Al-Cu4Mg1 alloy. The corrosion behaviour was assessed after exposition in the neutral salt spray of 5% NaCl aqueous solution. The weight losses were measured and calculated in g m<sup>-2</sup> and mm/year. The type of corrosion attack was observed by SEM on the cross-sectioned cuts. The corrosion products were analysed by local chemical analysis using SEM. Further, the corrosion resistance of Al alloy with protective coating were tested.

## INITIATION AND GROWTH OF FATIGUE CRACKS IN INCONEL 713LC WITH AL COATING AT 800 °C

SIMONA POSPÍŠILOVÁ<sup>a\*</sup>, KAREL OBRTLÍK<sup>b</sup>, MARTIN JULIŠ<sup>a</sup>, and TOMÁŠ PODRÁBSKÝ<sup>a</sup>

<sup>a</sup> Brno University of Technology, Technická 2896/2, 616 69 Brno, <sup>b</sup> Institute of Physics of Materials, Academy of Sciences of the Czech Republic, Žitkova 22, 616 62 Brno, Czech Republic  
pospisilova@fme.vubr.cz

Keywords: low cycle fatigue, IN713LC, aluminide coating, crack initiation, crack propagation rate

### 1. Introduction

Ni-based superalloy IN713LC is used for gas turbine integral wheels in aircraft industry. The high temperature components are exposed to high temperature fatigue and creep and their interactions, high-temperature oxidation and corrosion in aggressive environment. Protective coatings are used to improve high temperature performance<sup>1</sup>. Low cycle fatigue and high cycle fatigue of the material were studied rarely<sup>2,3</sup>. The diffusion coatings do not affect the creep life of Ni-based superalloys<sup>4</sup> but the effect on the fatigue life depends on number of factors<sup>5</sup>. Both the positive and detrimental effect of coatings was observed.

The aim of the present work is to study the fatigue crack initiation and propagation in superalloy IN713LC with Al coating and without coating at 800 °C. Microstructure characteristics and microhardness of Al coating are documented. Fatigue crack propagation rates from striation spacing observed on fatigue fracture were correlated with the stress intensity factor.

### 2. Experimental details

The chemical composition of experimental material is following: 0.04 % C; 11.85 Cr; 0.72 % Ti; 5.80 % Al; 2.27 % Nb; 4.54 % Mo; < 0.05 % Mn, Co, Ta; rest Ni.

Low cycle fatigue (LCF) tests were performed on button-end specimens having gauge length and diameter of 15 and 6 mm. The Al diffusion coating was applied to one half of specimens (on the gauge length) by out of pack technique at 1050 °C for 5 hours. Next samples were used without the protected coating. All specimens were fatigued in a computer controlled electro-hydraulic testing system at total strain rate of 0.002 s<sup>-1</sup> with fully reversed total strain cycle ( $R_\epsilon = -1$ ) at 800 °C in air. Based on previous research<sup>3</sup> it was found that the application of the Al diffusion coating results in changes of the fatigue behaviour of Inconel 713LC. Particularly, the stress response and the fatigue life of the coated material are different from those of the uncoated material. Light microscopy (LM) and scanning electron microscopy (SEM) were used

to study fracture surface and specimen sections. The microstructure, microhardness, and thickness of the coating were obtained. The fatigue crack propagation rate was estimated from the striation spacing in fracture surfaces.

### 3. Experimental results and discussion

The microstructure of Al coating is documented in Fig. 1 that shows the fracture surface at the specimen surface. The Al diffusion coating consists of the outer layer (OL) and the diffusion layer (DL). The thickness of the coating and the diffusion zone in as-coated state was 45–70 μm and 20–25 μm, respectively. The average microhardness of the outer layer and the diffusion layer in as-coated state was 512HK0.1 and 610HK0.1 (the Knoop microhardness test, load 0.1 kg), respectively.

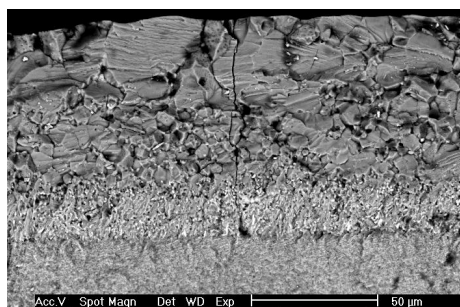


Fig. 1. Detail of Al coating on fracture surface (SEM)

The fracture surface of all studied samples is relatively rugged. The casting defects, most often shrinkage pores (up to 0.4 mm in diameter) occurred in fracture surfaces. In all cases, the fatigue crack initiation was observed at the surface both of coated and uncoated specimens. It was accelerated by shrinkage pores and carbides. Striations were observed in fatigue fractures in all specimens. Comparatively high incidence of carbides (type MC) was observed both in the fatigue fracture and final unstable fracture. The number of initiated cracks increases with growing plastic strain amplitude.

The fatigue crack shape was approximated by a semi-elliptical surface crack with a maximum crack depth  $b$  and surface crack length  $2a$ . Fatigue crack propagation rate  $db/dN$  was determined by assuming that each striation corresponds to a load cycle. Then, the distance between neighbouring striations  $s$  is equal to  $db/dN$ , where  $b$  is the crack length and  $N$  is the number of elapsed cycles.

Fatigue crack propagation rate was correlated with stress intensity factor amplitude  $K_{al}$ . To evaluate stress intensity factor, the linear elastic fracture mechanics was applied. The specimens with the total strain amplitudes  $\epsilon_a$  (0.43 and 0.45 %) were chosen, see Tab. I. The stress intensity factor amplitude  $K_{al}$  was obtained from equation (1)<sup>6</sup> valid for semi-elliptical surface crack in the round bar under uniform ten-

Table I  
The calibration function  $F_I$  and parameters of LCF

Specimen	$\varepsilon_a$ [%]	$\sigma_a$ [MPa]	$N_f$	$b/r$	$b/a$	$F_I$
1	0.45	582	397	0.08	1.23	0.65
2a*	0.43	651	195	0.33	0.54	0.89
2b*	0.43	651	195	0.52	0.9	0.72

\*a,b are two cracks in the same specimen

sion.  $\sigma_a$  is the remote stress amplitude and  $F_I$  is the dimensionless stress intensity factor (the calibration function).  $F_I$  depends on the ratio  $b/r$  and  $b/a$  where  $r$  is the specimen radius.  $F_I$  shown in Tab. I was obtained using the data<sup>6</sup> for the crack depth corresponding to the striation location.

$$K_{al} = F_I \sigma_a \sqrt{\pi \cdot b} \quad (1)$$

$$\frac{db}{dN} = AK_{al}^m \quad (2)$$

$$N = \frac{1}{A \cdot (\sigma_a F_I \cdot \sqrt{\pi})^m} \left( \frac{b_f^{1-\frac{m}{2}} - b_i^{1-\frac{m}{2}}}{1-\frac{m}{2}} \right) \quad (3)$$

Fatigue crack propagation rate  $db/dN$  versus stress intensity factor range  $\Delta K$  ( $2 K_{al}$ ) is plotted in Fig. 2. The crack propagation rate (square symbols in Fig. 2) were approximated using the Paris-Erdogan law (2) and material parameters  $A = 5.4 \cdot 10^{-9} \text{ m cyclus}^{-1} (\text{MPa m}^{1/2})^{-m}$  and  $m = 2.2$  were evaluated with regression analysis.

It is noted that crack growth data found from striation spacing correspond well with literature data obtained in CT specimens of superalloy IN 713C at 600 °C at R=0 (ref.<sup>7</sup>) (dashed line in Fig. 2). The crack propagation data of the present work are also in a good agreement to fatigue crack propagation rates of surface cracks acquired from cylindrical samples at 600 °C (ref.<sup>7</sup>).

The number of cycles necessary to semi-elliptical surface crack extension from the initial crack depth  $b_i$  to the final crack depth  $b_f$  was determined from equation (3) based on the integration of the relation (2) using (1). The initial crack depth is equal to the defect size observed on the fracture surface.  $b_f$  is the crack depth at the fatigue failure. The calculation shows that 300 cycles (76 % of fatigue life) are needed for crack propagation in specimen 1. Similarly, fatigue cracks propagates 127 cycles (65 % of fatigue life) in specimen 2. It means, major part of the fatigue life of specimens is spent in fatigue crack propagation from surface defects.

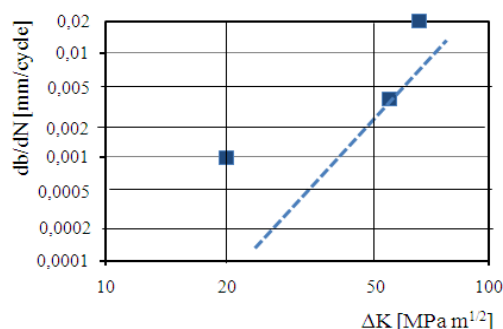


Fig. 2.  $db/dN$  versus  $\Delta K$  for material IN713LC at 800 °C (squares, present work) and for IN713C at 600 °C (dash line)<sup>7</sup>

#### 4. Summary

The fatigue crack initiation was observed on the free surface both in coated and uncoated specimens. The fatigue crack propagation rates determined from striation spacing can be approximated by the Paris-Erdogan law.

Research was supported by Czech Science Foundation (project 106/09/P522 and P107/11/2065), Ministry of Education, Youth and Sports (project MEB0810123), Brno University of Technology (project of specific research FSI-S-10-46), Ministry of industry and Trade (project FR-TII/099).

#### REFERENCES

- Čelko L., Klakurková L., Švejar J.: Mater. Manufacturing Processes 24, 1155 (2009).
- Juliš M., Obrtlík K., Pospíšilová S., Podrábský T., Polák J: Procedia Eng. 2, 1983 (2010).
- Obrtlík K. et al.: Key Eng. Mater. 452-453, 265 (2011).
- Juliš M., Pospíšilová S., Podrábský T.: Chem. Listy S/102, 880 (2008).
- Rahmani K., Nategh S.: Mater. Sci. Eng. A486, 686 (2008).
- Murakami Y.: Stress Intensity Factors Handbook. pp 659-665. Pergamon Books Ltd, 1987.
- Sonsino C. M., Brandt U., Bergmann J.: Elsevier Applied Science, London and New York 1992.

S. Pospíšilová<sup>a</sup>, K. Obrtlík<sup>b</sup>, M. Juliš<sup>a</sup>, and T. Podrábský<sup>a</sup> (<sup>a</sup> Brno University of Technology, <sup>b</sup> Institute of Physics of Materials AS CR): **Initiation and Growth of Fatigue Cracks in Inconel 713LC with Al Coating at 800 °C**

This paper is focused on the study of initiation and growth of fatigue cracks in IN713LC with Al protective coating and without coating. Microstructure characteristics and microhardness of Al coating are documented. Fatigue crack initiation and fatigue crack growth mechanisms were identified. The crack propagation rates were obtained based on striation spacing in fracture surfaces.